Scaling Behavior of Magnetoresistance with the Layer Number in CrI$_3$ Magnetic Tunnel Junctions

Baochun Wu,[1] Jie Yang,[1] Ruge Quhe,[2] Shiqi Liu,[1] Chen Yang,[1] Qiuhui Li,[1] Jiachen Ma,[1]
Yuxuan Peng,[1] Shibo Fang,[1] Junjie Shi,[1,5] Jinbo Yang,[1,3,4,5,*] Jing Lu,[1,3,4,5,6,†] and Honglin Du[1,3,4,‡]

[1] *State Key Laboratory for Mesoscopic Physics and School of Physics, Peking University, Beijing 100871, People's Republic of China*

[2] *State Key Laboratory of Information Photonics and Optical Communications and School of Science, Beijing University of Posts and Telecommunications, Beijing 100876, People's Republic of China*

[3] *Collaborative Innovation Center of Quantum Matter, Beijing 100871, People's Republic of China*

[4] *Beijing Key Laboratory for Magnetoelectric Materials and Devices (BKL-MEMD), Peking University, Beijing 100871, People's Republic of China*

[5] *Peking University Yangtze Delta Institute of Optoelectronics, Nantong 226010, People's Republic of China*

[6] *Key Laboratory for the Physics and Chemistry of Nanodevices and Department of Electronics, Peking University, Beijing 100871, People's Republic of China*

Two-dimensional (2D) van der Waals (vdW) magnetic semiconductors have attracted wide interest for their promising application in next-generation spintronic devices. We investigate the scaling behavior of the tunnel magnetoresistance (TMR) of the Ag/n-layer CrI$_3$/Ag and graphite/n-layer CrI$_3$/graphite magnetic tunnel junctions (MTJs) by using *ab initio* quantum-transport simulations. The calculated monotonic increasing TMR of the graphite/n-layer CrI$_3$/graphite MTJ with $n = 2$–4 at zero bias agrees with the experimental value. The TMR of the Ag/n-layer CrI$_3$/Ag MTJ generally increases with the tunnel-barrier layer number, n, that is, from 200% (2-layer CrI$_3$) to a record 10^9% value (12-layer CrI$_3$) at zero bias but has an odd-even oscillation when $n < 7$. When we apply a bias voltage to the Ag/2-layer CrI$_3$/Ag MTJ, the TMR first decreases slightly and then increases, followed by a monotonic decrease. The noncollinear magnetization direction of the CrI$_3$ layers also changes the TMR value of the graphite/n-layer CrI$_3$/graphite MTJ relative to the collinear case, a result in agreement with experiments.

I. INTRODUCTION

Traditional magnetic tunnel junctions (MTJs) are typically composed of two magnetic metallic electrodes separated by a nonmagnetic insulating spacer. MTJs based on the MgO spacer have a giant tunneling magnetoresistance (TMR) of up to 600% at room temperature by changing the relative magnetization orientations of the two magnetic electrodes, leading to very different bias outputs when a detection current is applied [1]. Nowadays, MTJs have already been widely used in the field of spintronics, such as the magnetic head of hard disk drives (HDDs), magnetic sensors, magnetic random-access memory, high-frequency oscillators, magnetic logic devices, spin field-effect transistors, and spin-torque diodes [2–10].

Taking the magnetic head of a HDD, for example, the whole history of development has gone through several

---

*jbyang@pku.edu.cn
†jinglu@pku.edu.cn
‡duhonglin@pku.edu.cn

stages, including anisotropic magnetoresistance (AMR) [11], giant magnetoresistance (GMR) [12], and TMR [1,13,14]. AMR is mainly achieved by the sensing layer made of anisotropic magnetic thin films in the magnetic head. GMR and TMR are achieved in similar sandwich structures, but the space layers of GMR devices are nonmagnetic conductors. Due to the low AMR value (1%–2%), the bias output shrinks below the bias drop of the leads when the size of the magnetic head becomes smaller, resulting in a low signal-to-noise ratio (SNR), a low sensitivity, and thus a low storage density ($\sim$1 GB/in.^{2}) [15,16]. The discovery of GMR (10%–20% at room temperature) increases the magnetoresistance (MR) by an order of magnitude, and hence, the bias output is greatly amplified when GMR-based MTJs are applied in the magnetic head. Therefore, a smaller change of the stored magnetic field can be detected, and the storage unit of the disk can be reduced in size. As a result, the storage density of the disks increases to about 300 GB/in^2. Afterward, the TMR observed in the MTJs that use Al$_2$O$_3$ ($\sim$20% at room temperature) and MgO ($\sim$600% at room

temperature) as tunnel barriers further helps to improve the detecting sensitivity and SNR of the magnetic head, thus leading to an ultrahigh storage density ($\sim$800 GB/in.^{2}) [1,14]. The MgO-based MTJs are now widely adopted in the magnetic heads of high-density magnetic recording hard disks.

In addition to the introduction of metal oxides as a tunneling barrier, another advance of great significance to traditional MTJs is the introduction of nonmagnetic semiconductors with a strong spin-orbit interaction (especially III-V semiconductors) as the tunnel barrier. Theoretically, the spin-dependent tunneling through the nonmagnetic semiconductor barrier is fully studied [17–21]. In nonmagnetic-semiconductor-based MTJs, a large difference in the tunneling transparency of the barrier for electrons in the two opposite spin states is obtained due to spin-orbit coupling at the interfaces. This leads to a strong spin polarization of the electrons after tunneling through the barriers for the initially unpolarized electrons and leads to the dependence of the TMR on the mean spin of the spin-polarized electrons injected into the MTJ. Moser *et al.* experimentally studied the TMR of the Fe/GaAs/Au MTJ and obtained similar results to the theoretical predictions [22]. In general, such nonmagnetic-semiconductor-based MTJs are also of interest for the development of devices for the processing of information stored in the magnitudes of the spin polarization of electrons in memory cells.

Recently, the discovery of two-dimensional (2D) intrinsic magnets and their application in MTJs have pushed the MR-improvement process one step further [23–28]. Thus, one of the most remarkable developments is the CrI_3-based MTJ with graphite electrodes. Several research groups have reported very large TMR in this system. Klein *et al.* observed TMR values of about 95%, 300%, and 550% in the 2-layer, 3-layer, and 4-layer CrI_3 MTJs at 300 mK under zero bias voltage with magnetization perpendicular to the plane [29]. Song *et al.* reported larger TMR values of about 310% (530%), 2000% (3200%), and 8600% (19 000%) in the 2-layer, 3-layer, and 4-layer CrI_3 MTJs at 2 K under about 0.3 V bias voltage with magnetization perpendicular (parallel) to the plane [30]. Kim *et al.* observed a surprising TMR of 10^6% in the 10-layer CrI_3 MTJ at 1.4 K under 0.4 V bias voltage with perpendicular magnetization [31], which is much larger than the maximum value ($\sim$1000%) of the traditional MTJs. Hence, the CrI_3-based MTJs have much higher detecting sensitivity and potential for achieving a larger storage density when applied in hard disk drives if the problems of low Curie temperature and high transition magnetic field are solved. The atomic thinness of the CrI_3 barrier layers can also minimize the device's size, and the tunability of the magnetic property of CrI_3 purely by an external electric field also means low operation energy in these MTJs [26,32–35].

Notably, the CrI_3-based MTJs are composed of two graphite electrodes separated by CrI_3 layers, and the resistance of this kind of MTJ depends significantly on the relative magnetization orientations of the tunnel-barrier layers (CrI_3 layers), rather than the relative magnetization orientations of the two electrodes in traditional MTJs. In such a MTJ configuration, the MR can be easily controlled by the number of layers of CrI_3. Although the MRs of the 2-layer, 3-layer, 4-layer, and 10-layer CrI_3-based MTJs with graphite electrodes have been measured and show an increasing tendency, TMR data in other layers are missing. Thus, one question remains open: what is the scaling behavior of the TMR with the number of layers in those missing layer numbers?

Here, we investigate the scaling behavior of the TMR of the Ag/n-layer CrI_3/Ag and graphite/n-layer CrI_3/graphite MTJs by using *ab initio* quantum-transport simulations. The calculated monotonic increasing TMR of the graphite/n-layer-CrI_3/graphite MTJ with $n = 2$–4 at zero bias is in agreement with the experimental value. Complete TMR data of the Ag/n-layer CrI_3/Ag MTJ at zero bias from $n = 2$ to 12 are established. It generally increases with the tunnel-barrier layer number, n, from 200% (2 layer) to a record 10^9% value (12 layer) at zero bias. This surprising TMR is the largest value among all theoretical reports on the 2D MTJ configuration with several tunnel layers [34,36–39]. More interestingly, unexpected odd-even oscillations of the total conductance, spin polarization, and TMR are observed when $2 \leq n \leq 12$ for the first two physical quantities and $2 \leq n \leq 7$ for the last one. By contrast, no such oscillation is observed for the graphite/n-layer CrI_3/graphite configuration. Additionally, the effects of the applied bias voltage and the magnetization orientation of the CrI_3 layers on the TMR are also investigated quantitatively. When we apply a bias voltage to the Ag/2-layer CrI_3/Ag MTJ, the TMR first decreases slightly and then increases, followed by a monotonic decrease. The noncollinear magnetization direction of the CrI_3 layers also alters the TMR value of the graphite/n-layer CrI_3/graphite MTJ relative to the collinear case, a result in agreement with experiments.

II. COMPUTATIONAL METHOD

The electronic structure calculations of n-layer CrI_3 are carried out using the projector augmented wave method with the Perdew-Burke-Ernzerhof (PBE) generalized gradient approximation (GGA) [40], as implemented in the VASP package [41–43]. The energy cutoff is 400 eV for the plane-wave basis expansion with the total energy convergence criteria of 1×10^{-4} eV per unit cell. The Monkhorst-Pack k-point mesh is sampled with a separation of about 0.01 Å^{-1} in the 2D Brillouin zone. The ionic relaxation for structure optimization stops when the residual force on each atom is less than 0.01 eV·Å^{-1}. The vdW-D2 approach

is adopted to describe the interlayer van der Waals (vdW) interaction. The Hubbard U value is set as zero because previous results have shown that the U value has little effect on the band gaps of monolayer CrI$_3$ [44].

For the MTJs, the spin-resolved transport characteristics are simulated by using density-functional theory (DFT) coupled with the nonequilibrium Green's function formalism, as implemented in the Atomistix ToolKit 2018 software package [45,46]. The exchange-correlation interaction here is represented by the spin-polarized generalized gradient approximation in the form of the PBE potential. The real-space density mesh cutoff is taken as 60 hartree. The double-zeta-polarized set is used. The boundary conditions are period-, period-, and Dirichlet-type conditions along x, y, and z directions (z is the transport direction), respectively. The k-point meshes for the electrode region and the central region are $10 \times 10 \times 20$ and $10 \times 10 \times 1$, respectively. In addition, all of our calculations are performed at 0 K.

In our calculations, the spin-resolved transmission coefficient, $T_\sigma^{k_\parallel}(E)$ ($k_\parallel$ stands for the reciprocal lattice vector along the surface-parallel direction in the irreducible Brillouin zone, σ is the spin index), is represented by [47–49]

$$T_\sigma^{k_\parallel}(E) = \text{Tr}[\Gamma_{l,\sigma}^{k_\parallel}(E) \, G_\sigma^{k_\parallel}(E) \, \Gamma_{r,\sigma}^{k_\parallel}(E) \, G_\sigma^{k_\parallel \dagger}(E)], \quad (1)$$

where $G_\sigma^{k_\parallel}(E)$ and $G_\sigma^{k_\parallel \dagger}(E)$ stand for the retard and advanced Green's function, respectively.

$$G_\sigma^{k_\parallel}(E) = \left[(E + i\delta_+)I_\sigma^{k_\parallel} - H_\sigma^{k_\parallel} - \sum_{l,\sigma}^{k_\parallel}(E) - \sum_{r,\sigma}^{k_\parallel}(E)\right]^{-1},$$

where δ_+ is an infinitesimal positive number, $I_\sigma^{k_\parallel}$ is the identity matrix, $H_\sigma^{k_\parallel}$ is the Hamiltonian matrix, and $\sum_{l/r,\sigma}^{k_\parallel}(E)$ is the self-energy matrix. $\Gamma_{l/r,\sigma}^{k_\parallel}(E) = i(\sum_{l/r,\sigma}^{k_\parallel} - \sum_{l/r,\sigma}^{\dagger k_\parallel})$ is the broadening width originating from the left or right electrode in the form of self-energy $\sum_{l/r,\sigma}^{k_\parallel}$. Given a certain energy, the transmission function, $T_\sigma(E)$, is obtained by averaging the transmission coefficient, $T_\sigma^\parallel(E)$, over all different $k_\parallel$. The spin-resolved drain current, I_σ, is obtained through the following Landauer-Büttiker formula [50,51]:

$$I_\sigma(V_b, V_g) = \frac{e}{h} \int_{-\infty}^{+\infty} \{T_\sigma(E, V_b, V_g)[f_S(E - \mu_S) - f_D(E - \mu_D)]\}dE, \quad (2)$$

where f_S and f_D are the Fermi-Dirac distribution functions for the source and drain, respectively; μ_S and μ_D are the Fermi levels of the source and drain, respectively; and V_b

and V_g are the bias voltages of the two electrodes and the gate voltage, respectively. The spin orientation of the Cr atoms is initially set as the out-of-plane direction, which is also the easy axis of the CrI$_3$ layers, unless otherwise specified.

III. RESULTS AND DISCUSSION

A. Electronic structures of *n*-layer CrI$_3$

The side and top views of the atomic structure of 2-layer CrI$_3$ are shown in Figs. 1(a) and 1(b), respectively. According to the experimental results, the ground magnetic state of 2-layer CrI$_3$ is set as the *A*-type antiferromagnetic state with an out-of-plane easy axis, featuring intralayer ferromagnetic (FM) coupling and interlayer antiferromagnetic (AFM) coupling [26]. The optimized distance between the two layers is $d_0 = 3.39$ Å. We first calculate the spin-resolved band structure of monolayer CrI$_3$ in the FM ground state. We find that the smaller band gap of the majority-spin electrons is $\Delta_s = 1.13$ eV, and the larger band gap of the minority-spin electrons is $\Delta_l = 1.99$ eV. Then we calculate the spin-resolved AFM and FM band structures of 2-layer CrI$_3$, which are shown in Figs. 1(c) and 1(d), respectively. In the interlayer AFM-coupled state, the smaller band gap degenerates for two spins coming from the different layers with $\Delta_s^{\uparrow\downarrow} = 1.13$ eV. The larger band gap is also degenerate for two spins coming from different layers with $\Delta_l^{\uparrow\downarrow} = 2.02$ eV. In the interlayer FM-coupled state, the smaller band gap is slightly reduced to $\Delta_s^{\uparrow\uparrow} = 0.99$ eV, which comes from the weak coupling of the spin-up electrons of the 2 layers, and the larger band gap is slightly reduced to $\Delta_l^{\uparrow\uparrow} = 1.94$ eV, due to the weak coupling of the spin-down electrons of the 2 layers. $\Delta_s^{\uparrow\downarrow}$ and $\Delta_s^{\uparrow\uparrow}$ are close to the previous calculation results [52] but slightly smaller than the experimental doped band gap of 1.24 eV measured on cleaved bulk CrI$_3$ in the FM ground state by angle-resolved photoemission spectroscopy [53], due to neglecting the many-body effect in the standard DFT approach. When the CrI$_3$ layers pile up in a FM order, the majority-spin electrons and minority-spin electrons will encounter a small and a large tunnel-barrier heights in both layers, respectively. The total resistance is dominated by the small tunnel-barrier height and has a small value. By contrast, when the CrI$_3$ layers pile up in an AFM order, both spins will encounter a larger tunnel-barrier height in either layer. Thus, the total resistance will have a large value.

To consider the layer-related effect, we also calculate the spin-resolved AFM and FM band structures of *n*-layer ($n = 3$–8) and bulk CrI$_3$ for comparison. Figures 1(e) and 1(f) display the spin-resolved band structures of 3-layer CrI$_3$, representing the odd layers. The band structures of 2-layer and 3-layer CrI$_3$ in the FM state are very similar, and the band gaps are also nearly the same. As
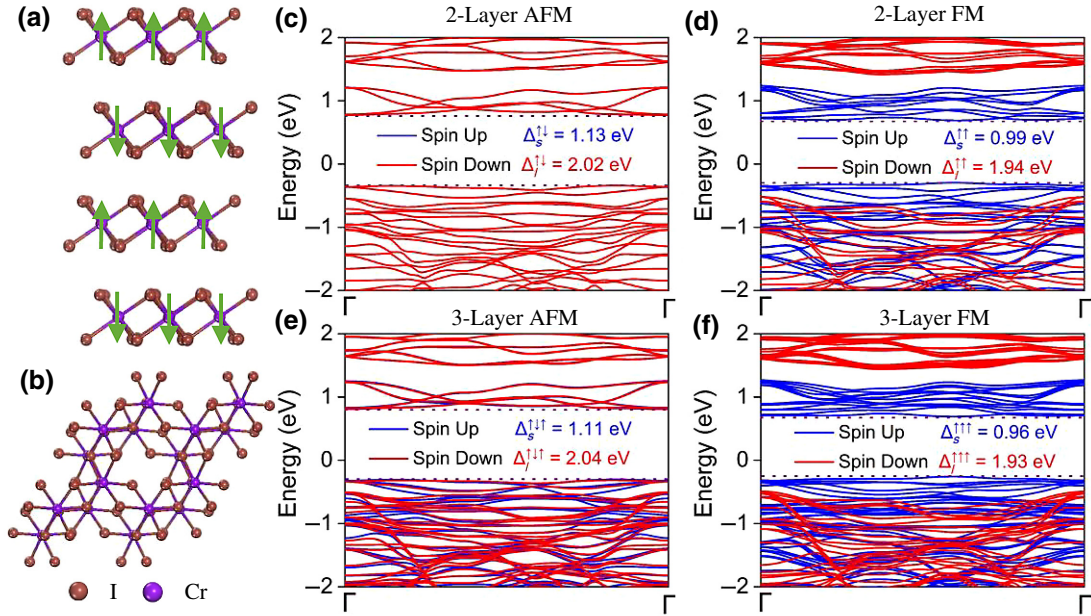
FIG. 1. Side (a) and top (b) views of the atomic structure of 2-layer CrI₃. Arrows represent the magnetic moments in each layer. Spin-resolved band structures of AFM (c) and FM (d) 2-layer CrI₃. Spin-resolved band structures of AFM (e) and FM (f) 3-layer CrI₃. Fermi level is set to zero. Band gaps of different spins are indicated.

for the AFM state, the bands of the spin-up and spin-down electrons in the 2-layer CrI₃ coincide entirely, while the bands of the spin-up and spin-down electrons in the 3-layer CrI₃ are slightly different, which is due to different spin-up and spin-down layer numbers. Figure 2 summarizes the layer dependence of the spin-resolved band gaps of the n-layer CrI₃. We can see that the variation tendency of the band gaps with increasing number of layers is not simply a monotonous one, as the case of 2D black phosphorus [54]. Δ_s and Δ_l of the FM state both first decrease with increasing n, and reach a minimum when $n = 6$, before they start to increase with n. The whole tendency is like the case of 2D Bi₂O₂Se [55]. Δ_s and Δ_l of the AFM state keep going up and down around certain energy levels until
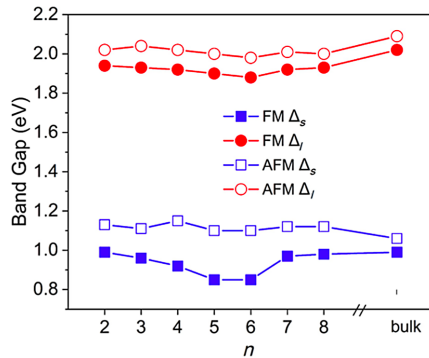
they reach the bulk value. It is worth noting that the variation range of all spin-resolved band gaps is relatively small (less than 0.2 eV), indicating a weak coupling between CrI₃ layers [53,56].

B. Transport properties of the CrI₃-based MTJs

1. TMR of the out-of-plane-magnetized Ag/n-layer CrI₃/Ag MTJ at zero bias

We use n-layer CrI₃ with layer number, n, ranging from 2 to 12 to connect the Ag (111) surface to build the Ag/n-layer CrI₃/Ag MTJs, as shown in Fig. 3(a). The noble-metal Ag is selected for the electrodes because of a small lattice mismatch with CrI₃, a relatively small work function, and a low Schottky barrier height, which leads to better performance in the MTJ [4]. The optimized distance between Ag (111) and the adjacent CrI₃ layer is 2.71 Å with minor structure distortion during the relaxation process. At the interface, we can see that Ag and I atoms form covalent bonds with a bond length of 2.95 Å, which indicates that iodine is likely to form compounds with noble metals represented by Ag. Meanwhile, the distance between CrI₃ layers increases from 3.39 to 3.59 Å.

Then we simulate the transport properties of the MTJs. G_{FM} and G_{AFM} are defined as the conductance of the MTJs when CrI₃ layers are FM ordered and AFM ordered [Fig. 3(b)], respectively. G_{FM} and G_{AFM} are calculated at $E = E_f$ as

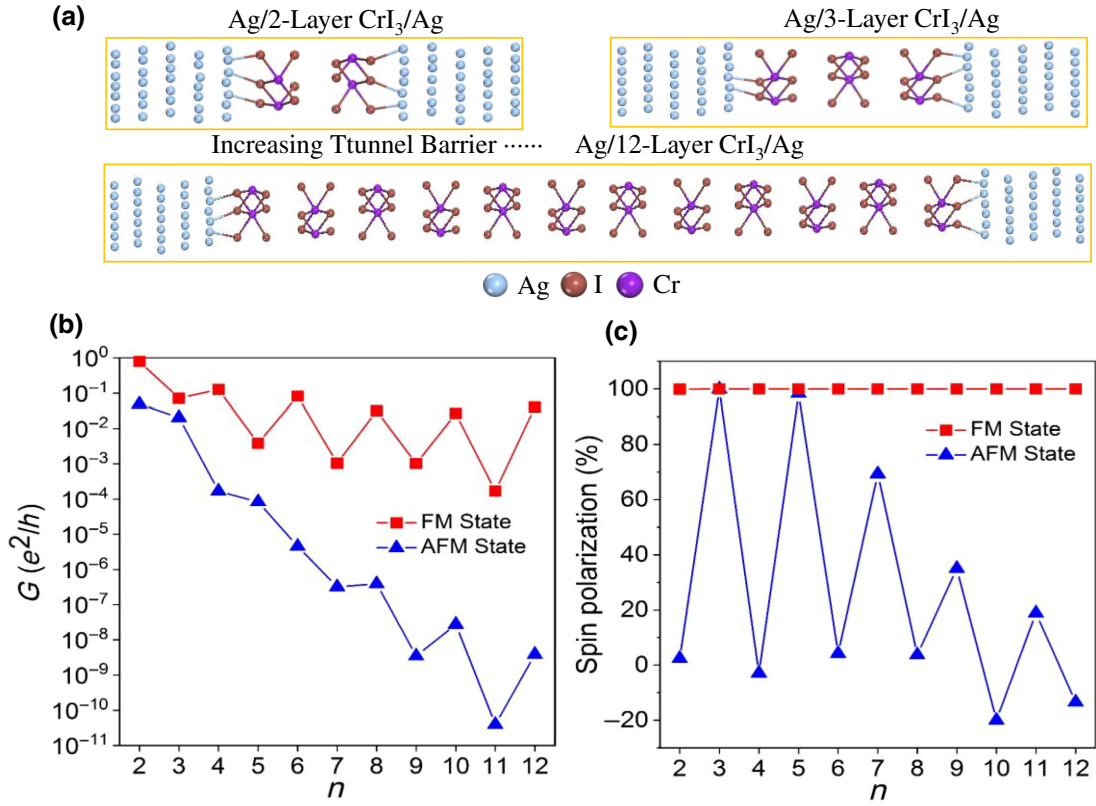$$G_{\text{FM}} = \frac{e^2}{h}[T_{\text{FM},\uparrow}(E) + T_{\text{FM},\downarrow}(E)], \qquad (3)$$

FIG. 2. Layer dependence of the spin-resolved band gaps of n-layer CrI₃.

FIG. 3. Ag/n-layer CrI$_3$/Ag magnetic tunnel junction. (a) Device model. (b and c) Layer number n dependent linear conductance (b) and spin polarization (c). All of the results listed above are with out-of-plane magnetization.

$$G_{\mathrm{AFM}} = \frac{e^2}{h}[T_{\mathrm{AFM},\uparrow}(E) \; + \; T_{\mathrm{AFM},\downarrow}(E)], \qquad (4)$$

where T_{FM} and T_{AFM} represent the transmission functions of the MTJs in the FM and AFM states, respectively. P_{FM} and P_{AFM} are defined as the spin polarization (P) of the MTJs when CrI$_3$ layers are FM ordered and AFM ordered [Fig. 3(c)]. At zero bias, P is calculated as

$$P_{\mathrm{FM}} = [T_{\mathrm{FM},\uparrow}(E) - T_{\mathrm{FM},\downarrow}(E)]/$$
$$\times [T_{\mathrm{FM},\uparrow}(E) \; + \; T_{\mathrm{FM},\downarrow}(E)], \qquad (5)$$
$$P_{\mathrm{AFM}} = [T_{\mathrm{AFM},\uparrow}(E) - T_{\mathrm{AFM},\downarrow}(E)]/$$
$$\times [T_{\mathrm{AFM},\uparrow}(E) \; + \; T_{\mathrm{AFM},\downarrow}(E)], \qquad (6)$$

at $E = E_f$. The value of P directly reflects the spin-filtering effect in the MTJs. As mentioned above, the spin-dependent band gaps of n-layer CrI$_3$ lead to spin-dependent tunnel-barrier heights in CrI$_3$ MTJs. Specifically, when the MTJ is in the FM state, the spin-up electrons (defined as the majority electrons) encounter a low tunnel barrier in every CrI$_3$ layer, and hence, can mostly tunnel through the barrier. On the other hand, the spin-down electrons (defined as the minority electrons) encounter a high tunnel barrier in every CrI$_3$, and hence,

can hardly tunnel through the barrier. Taking the two situations together, we can conclude that the tunneling process in the FM-ordered MTJ is dominated by the majority electrons that encounter a low barrier, thus resulting in a high G_{FM} and P_{FM}. As for the AFM-ordered MTJ, the whole system is symmetric, and the situation is the same for electrons of both spins. They both encounter a high tunnel barrier when tunneling through CrI$_3$ layers that possess opposite spin, thus resulting in a low G_{AFM} and P_{AFM}. As shown in Figs. 3(b) and 3(c), for the same layer number, n, G_{FM} is generally several orders of magnitude larger than G_{AFM}, and P_{FM} is also larger than P_{AFM}, except for $n = 3$ and $n = 5$, where both P_{FM} and P_{AFM} approximate 100%. The reason why there are special cases involves the modification of the spin-filtering model and will be discussed later. Now, we focus on layer-related behavior.

As shown in Fig. 3(b), generally speaking, G_{FM} and G_{AFM} both tend to decrease with n, and the latter falls more sharply. This is comprehensible, as each additional layer acts as another spin filter and reduces the number of electrons that can tunnel through. Additionally, the spin-filtering effect suppresses the transmission of both majority- and minority-spin electrons in the AFM configuration, while it allows a transport channel for majority-spin electrons in the FM configuration. What is more interesting is that, for G_{FM}, the scaling behavior exhibits odd-even

oscillation from $n = 2$ to $n = 12$, while, for G_{AFM}, it monotonously decreases when $n < 7$ and exhibits odd-even oscillation from $n = 7$ to $n = 12$. The calculated G_{FM} of the Ag/4-layer CrI$_3$/Ag MTJ ($\sim 10^{-1}$ e^2/h) here is 2 orders of magnitude larger than the previously reported G_{FM} of the Cu/4-layer CrI$_3$/Cu MTJ (10^{-3} e^2/h) [36], indicating that the Ag electrodes are better for electron transport, probably because of the smaller work function and lower Schottky barrier height mentioned above. Meanwhile, our calculated G_{FM} of the Ag/2-layer CrI$_3$/Ag MTJ ($\sim 10^{-1}$ e^2/h) is 5 orders of magnitude larger than the previously reported G_{FM} of the Ag/CrI$_3$/h-BN/CrI$_3$/Ag MTJ (10^{-6} e^2/h), and our calculated G_{AFM} of the Ag/2-layer CrI$_3$/Ag MTJ ($\sim 10^{-2}$ e^2/h) is also 5 orders of magnitude larger than G_{AFM} of the Ag/CrI$_3$/h-BN/CrI$_3$/Ag MTJ (10^{-7} e^2/h) [4]. This indicates that the h-BN layer in the middle blocks the transport of electrons and this blocking is spin insensitive. It is also worth noting that G_{FM} of the Ag/n-layer CrI$_3$/Ag MTJ remains relatively large ($\sim 10^{-2}$ e^2/h), even when the layer number, n, is up to 12. We will talk about the reason later.

Meanwhile, as shown in Fig. 3(c), P_{FM} remains close to 100% from $n = 2$ to $n = 12$, indicating a perfect spin-filter efficiency (SFE) of the FM-ordered CrI$_3$ layers. The previously reported Cu/4-layer-CrI$_3$/Cu MTJ also exhibits nearly 100% P_{FM} [36]. Hence, the FM-ordered CrI$_3$ layers are an ideal spin-current source. On the contrary, P_{AFM} is related to the parity of the layer number. On the whole, the variation tendency exhibits odd-even oscillation. For the even layer numbers, P_{AFM} is randomly distributed around zero. For the odd layer numbers, P_{AFM} exhibits a monotonously decreasing tendency. Notably, when $n > 8$, the transmission function is less than 10^{-8} and the precision limit of the calculation is approached. So, the calculated P has a margin of error, which might account for the P_{AFM} that deviates from 0 when $n = 10$ and $n = 12$. The mechanism behind the behavior of P_{AFM} will be discussed later.

Figure 4 exhibits the spin-resolved transmission eigenstate at E_f and the Γ point in k space in the out-of-plane-magnetized Ag/4-layer CrI$_3$/Ag MTJ at zero bias in the FM and AFM states. We can see visually that, in the FM state, the spin-up electrons can mostly tunnel through the barriers and reach the other electrode, while the spin-down electrons are primarily blocked in the channel. In the AFM state, both the spin-up electrons and the spin-down electrons are primarily blocked in the channel.

We then calculate the TMR of the Ag/n-layer CrI$_3$/Ag MTJ at zero bias. From a practical point of view, when we apply a progressively increasing magnetic field to flip the magnetization of the AFM-ordered MTJ, the total conductance gradually increases and reaches a maximum when the magnetic field reaches the critical point. If the TMR in this dynamic process is defined as TMR = $[R(H) - R(0)/R(0)] \times 100\%$, where H is the strength of the external magnetic field, then TMR surely changes with H [31]. However, our static calculation focuses on the two stable states, that is, the initial AFM state and the final FM state. Thus, we use the definition TMR = $[(R_{AFM} - R_{FM})/R_{FM}] \times 100\%$ and do not include the effect of the external magnetic field that is applied during the dynamic process. Utilizing the reciprocal relationship between R and G, we can transform the definition into TMR = $[(G_{FM} - G_{AFM})/G_{AFM}] \times 100\%$. Figure 5 exhibits the variation tendency of the TMR with the layer number, n, in the Ag/n-layer CrI$_3$/Ag MTJ at zero bias. Compared with the previously calculated TMR of about 3000% for the Cu/4-layer -CrI$_3$/Cu MTJ, we obtain a much larger TMR value ($\sim 75\,000\%$) in the Ag/4-layer CrI$_3$/Ag MTJ, indicating that Ag is a better choice for the electrodes [36]. In addition, the calculated TMR of the Ag/2-layer CrI$_3$/Ag MTJ is about 1500%, which is very close to the previously calculated TMR of the Ag/CrI$_3$/h-BN/CrI$_3$/Ag MTJ ($\sim 1250\%$) [4]. We mention above that G_{FM} and G_{AFM} of our Ag/2-layer CrI$_3$/Ag MTJ are both 5 orders of magnitude larger than G_{FM}
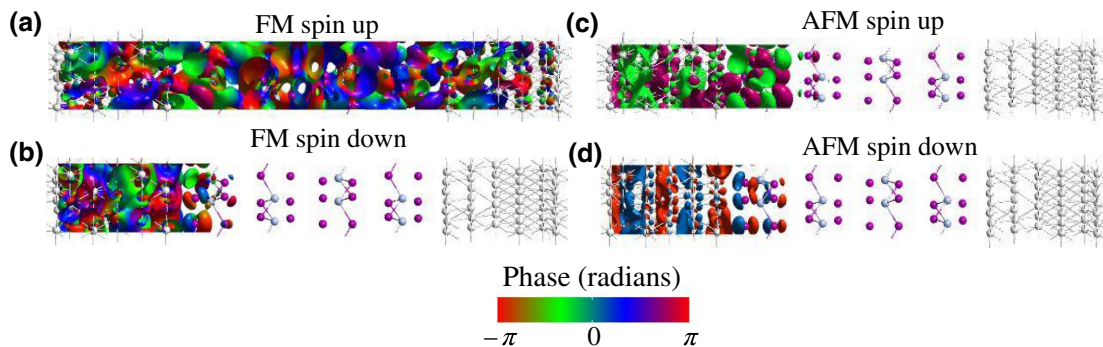

FIG. 4.   Spin-resolved transmission eigenstate at E_f and the Γ point in k space in the out-of-plane-magnetized Ag/4-layer CrI$_3$/Ag MTJ at zero bias. Isovalue is 0.1 arb. units.
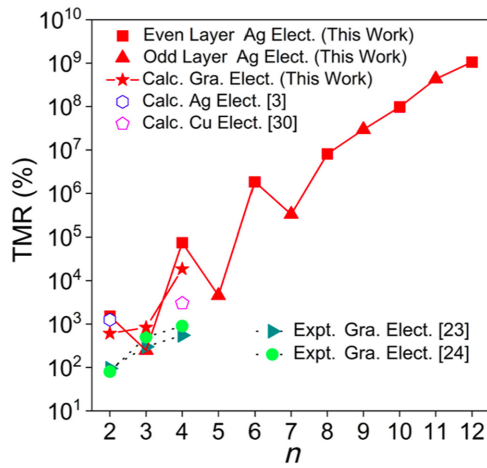
FIG. 5. Calculated TMR in a $\log_{10}$ scale of the Ag/n-layer CrI_3/Ag MTJs and the graphite/n-layer CrI_3/graphite MTJs. Previous calculations of CrI_3 MTJs with Ag and Cu electrodes and previous experiment results of CrI_3 MTJs with graphite electrodes are listed for comparison [3,23–25,30]. Thereinto, all the calculation results [3,30] and experiment results [23–25] are obtained under zero bias voltage. All of the results listed above are with out-of-plane magnetization.

and G_{AFM} of the Ag/CrI_3/h-BN/CrI_3/Ag MTJ due to the spin-insensitive blocking effect of the h-BN layer. Then, according to the definition of TMR, which can be written as TMR $= [(G_{FM} - G_{AFM})/G_{AFM}] \times 100\%$, if we multiply G_{FM} and G_{AFM} by the same factor (10^{-5}), TMR does not change. This explains the similar TMR results above. As for the overall scaling behavior of the TMR with the layer number, when $n < 7$, the variation tendency of the TMR ($10^2\%$–$10^6\%$) exhibits odd-even oscillation. That is, if we assume l is a positive integer and $2l < 7$, then we have $TMR_{2l} > TMR_{2l+1}$ (the subscript represents the corresponding layer number). Separately, for the odd layer numbers or even layer numbers, the TMR monotonously increases. When $n > 7$, the odd-even oscillation disappears and the TMR monotonously increases from $n = 7$ ($10^5\%$) to $n = 12$ ($10^9\%$).

It is noteworthy that the odd-even oscillation is not observed experimentally in the graphite/n-layer CrI_3/graphite MTJ, where the TMR monotonously increases from 95% at $n = 2$ and 300% at $n = 3$ to 550% at $n = 4$ with perpendicular magnetization orientation at zero bias voltage in Klein's experiment, and from 80% (50%) at $n = 2$ and 500% (500%) at $n = 3$ to 900% (600%) at $n = 4$ with perpendicular (parallel) magnetization orientation at zero bias voltage in Song's experiment [30,31]. For comparison, we also calculate the transport properties of the graphite/n-layer CrI_3/graphite MTJs from $n = 2$ to $n = 4$ with out-of-plane magnetization at zero bias. The corresponding TMR is 600%, 800%, and 18 000%, respectively. Notably, we do not choose the graphite-electrode configuration, in the first place, to study the

layer-dependent scaling behavior because the transmission function decreases sharply with layer number n (about 10^{-24} when $n = 4$) in our vertically stacked graphite-electrode MTJ model. When $n > 4$, the calculation is out of our precision. The monotonous increasing trend of the calculated TMR is consistent with the experimental results. Meanwhile, the monotonous increase of the TMR with layer number in the graphite/n-layer CrI_3/graphite MTJ indicates that the occurrence of the odd-even oscillation in the Ag/4-layer CrI_3/Ag MTJ originates from the choice of Ag electrodes, which we will explain in detail later.

2. Projected local density of states (PLDOS) of the out-of-plane-magnetized CrI_3-based MTJs at zero bias

a. Description and comparison of PLDOS figures.—To further understand the mechanism of the odd-even oscillation of the TMR with n and the generally increasing TMR with n, we plot the spin-resolved PLDOS for the graphite/n-layer-CrI_3/graphite MTJ and Ag/n-layer CrI_3/Ag MTJ ($n = 3, 4$) in the FM and AFM states, respectively, with out-of-plane magnetization at zero bias for comparison, as shown in Figs. 6 and 7. The spin-filtering effect existing in configurations of both electrodes and the tunnel barriers of every CrI_3 layer for both spins are directly visualized in the PLDOS figures. We can see clearly that electrons of different spins encounter tunnel barriers of different heights (yellow lines). The lower tunnel barrier corresponds to Δ_s in the spin-resolved band structure, and the higher tunnel barrier corresponds to Δ_l in the spin-resolved band structure.

One obvious feature is that the transport capacity of the graphite-electrode configuration is much weaker than the Ag-electrode configuration, especially near the Fermi level. For example, the transmission function at the Fermi level of the FM-ordered Ag/3-layer CrI_3/Ag MTJ is about 10^{-2}, while that of the FM-ordered graphite/3-layer CrI_3/graphite MTJ is about 10^{-20}. Graphene's unique dispersion near the Fermi level, which leads to a small electron density of states (DOS) at E_f, partly accounts for the extremely small transmission function. The increasing transmission function as the energy moves away from the Fermi level is also due to the augmented conical Fermi contour of the graphene electrodes. Another important factor for the huge difference in transmission is the interaction between the electrodes and the CrI_3 layers. The graphene electrodes hardly interact with the CrI_3 layers, whereas the interaction between the Ag electrodes and the CrI_3 layers is very strong. We can see an obvious increase in DOS near the Fermi level of the CrI_3 layers, especially the two CrI_3 layers adjacent to the electrodes. We call this the metallization effect of the Ag electrodes, as the increase in itinerant electrons near the Fermi level makes the CrI_3 layers behave more like magnetic metals. We will talk about
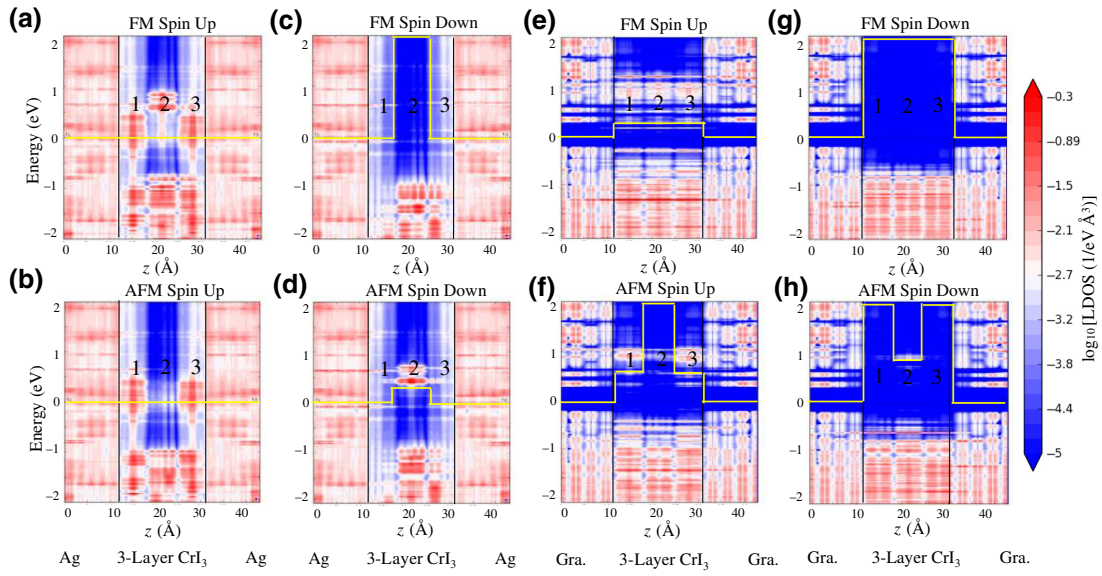
FIG. 6.   Spin-resolved PLDOS of the Ag/3-layer CrI$_3$/Ag and graphite/3-layer CrI$_3$/graphite MTJs for the AFM and FM states. Fermi level is set to zero energy. Black lines indicate the boundary lines of the electrode and tunnel region, and yellow lines are the spin-dependent potential-barrier profiles. Numbers indicate the corresponding CrI$_3$ layers.

this metallization effect in detail later, as it involves the modification of the simplest spin-filtering model. We first explain the general increasing tendency of the TMR under the framework of the simplest spin-filtering model.

b. Qualitative theoretical model explaining the increasing TMR.—The quantitative explanation for the generally

increasing TMR with *n* is similar to the strict theoretical derivation in recent work on the CrPS$_4$-based MTJ [49], where the Wentzel-Kramers-Brillouin (WKB) approximation is used, and a monotonously increasing cosh function relationship between TMR^{odd} (TMR^{even}) and tunnel-barrier thickness is obtained. Here, we try to give another more approximate explanation by making use of the PLDOS figures. In Figs. 6 and 7, we find
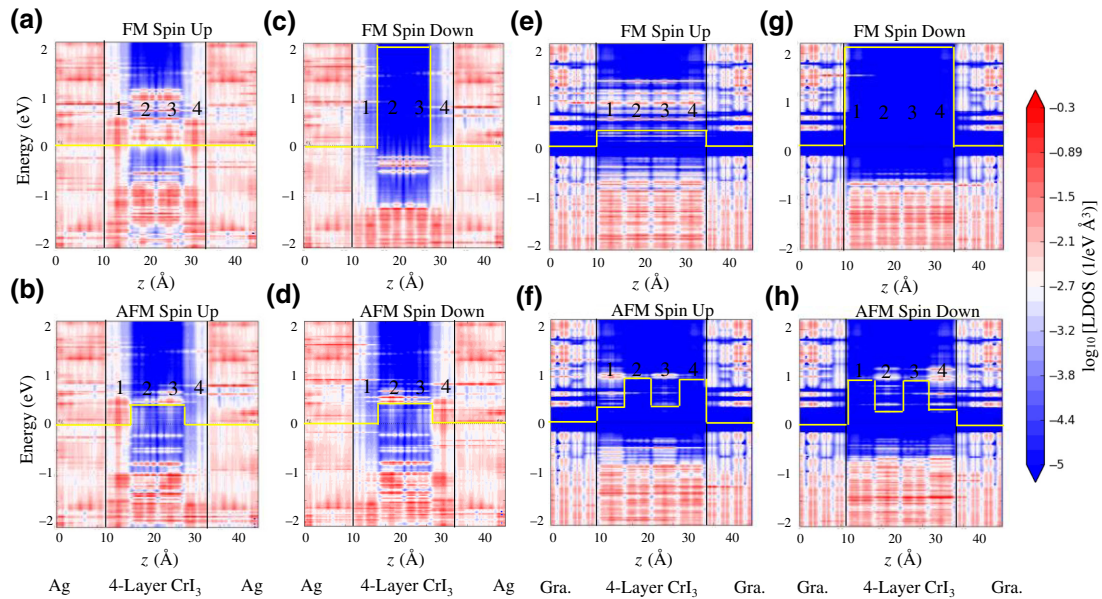

FIG. 7.   Spin-resolved PLDOS of the Ag/4-layer CrI$_3$/Ag and graphite/4-layer CrI$_3$/graphite MTJs for the AFM and FM states. Fermi level is set to zero energy. Black lines indicate the boundary lines of the electrode and tunnel region, and yellow lines are the spin-dependent potential-barrier profiles. Numbers indicate the corresponding CrI$_3$ layers.

that, for the tunnel barriers (marked with yellow lines), when n increases from three to four, the product of the height and length (defined as s) also increases proportionally. This proportional increase exists for every n from 2 to 12. According to the WKB formula, the tunneling transmission function (T) can be written as

$$T = \exp\left\{-4\int \frac{dx\sqrt{2\mu[U - E_f + B(x)\sigma]}}{\hbar}\right\}, \quad (7)$$

where $U - E_f$ is the tunnel-barrier height in the nonmagnetic system, μ is the effective mass of an electron in the band, $B(x)$ is the x-dependent magnetic field, σ is the spin index, and $\hbar$ is Plank's constant. $U - E_f + B(x)\sigma$ is equivalent to the height of the tunneling barrier in the magnetic system (defined as h). Notably, there is no tunnel barrier in the two electrodes, and the tunnel barriers in the central region can be divided into n discrete rectangles. So, if we introduce s here, we can get

$$T \approx \exp\left(-\frac{4\sqrt{2\mu}}{\hbar}\sum_{i=1}^{n}\sqrt{d}\sqrt{dh_i}\right)$$

$$= \exp\left(-\frac{4\sqrt{2\mu}}{\hbar}\sqrt{d}\sum_{i=1}^{n}\sqrt{s_i}\right), \quad (8)$$

where d is the distance from center to center of two adjacent CrI$_3$ layers, and i is the layer label. The conductance is given by

$$G = \frac{e^2}{h}\sum_{\sigma}T_\sigma. \quad (9)$$

Thus, we can get

$$G_{\text{FM}} = \frac{e^2}{h}(T_{\text{FM},\uparrow} + T_{\text{FM},\downarrow}), \quad (10)$$

$$G_{\text{AFM}} = \frac{e^2}{h}(T_{\text{AFM},\uparrow} + T_{\text{AFM},\downarrow}). \quad (11)$$

Since $T_{\text{FM},\uparrow} \gg T_{\text{FM},\downarrow}$ and $T_{\text{AFM},\uparrow} = T_{\text{AFM},\downarrow}$, we have

$$r(n) = \frac{G_{\text{FM}} - G_{\text{AFM}}}{G_{\text{AFM}}} \approx \frac{T_{\text{FM},\uparrow}}{2T_{\text{AFM},\uparrow}} - 1,$$

$$= \frac{1}{2}\exp\left[\frac{4\sqrt{2\mu}}{\hbar}\sqrt{d}\left(\sum_{i=1}^{n}\sqrt{s_{i,\text{AFM},\uparrow}}\right.\right.$$

$$\left.\left. - \sum_{i=1}^{n}\sqrt{s_{i,\text{FM},\uparrow}}\right)\right] - 1, \quad (12)$$

where $r(n)$ refers to the TMR of the MTJ with n-layer spacer. If we define B_i (C_i) as the area of each higher

(lower) tunnel barrier for the spin-up electrons in the AFM-ordered configuration, and D_i as the area of each tunnel barrier for the spin-up electrons in the FM-ordered configuration, then we have

$$s_i = dh_i \ (s_i = B_i, \ C_i, \text{ and } D_i). \quad (13)$$

For the sake of simplicity, we assume that B_i, C_i, and D_i are independent of i (like the case in the graphite-electrode configuration) and equals constant values of B, C, and D, respectively. Then we have

$$\sum_{i=1}^{n}\sqrt{s_{i,\text{AFM},\uparrow}} \approx \frac{n}{2}\left(\sqrt{B} + \sqrt{C}\right), \quad (14)$$

$$\sum_{i=1}^{n}\sqrt{s_{i,\text{FM},\uparrow}} = n\sqrt{D}. \quad (15)$$

So,

$$r(n) = \frac{1}{2}\exp\left[\frac{4\sqrt{2\mu}}{\hbar}\sqrt{d}\left(\frac{\sqrt{B} + \sqrt{C}}{2} - \sqrt{D}\right)n\right] - 1. \quad (16)$$

The values of B, C, and D can be seen in the PLDOS figures, and we have $B \geq D$ and $C \geq D$. Therefore, as n increases, the TMR also increases exponentially. Furthermore, if we assume $\mu \approx m_0$ (m_0 is the mass of the free electron), and we can get $B/d \approx 1$ eV, $C/d \approx 0.2$ eV, and $D/d \approx 0.2$ eV from Fig. 7 (the graphite-electrode case), then we have

$$r(n) \approx \frac{1}{2}\exp(1.92n) - 1. \quad (17)$$

We plot this model in Fig. 8 to make a comparison with our actual calculation results. We find that, when $n = 2, 4$,
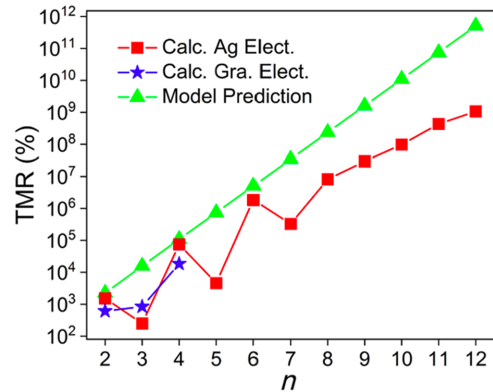

FIG. 8. Comparison of the predicted TMR of our model using WKB approximation with our actual calculated TMR in the out-of-plane-magnetized MTJs at zero bias.

and 6, the predicted TMR of this model is very close to our calculated TMR of the Ag-electrode configuration at zero bias. In other cases, there is a deviation between the model and actual calculated value, since B_i, C_i, and D_i are dependent on layer label i and total layer number n, and cannot be seen as constant values, especially at the boundary adjacent to the Ag electrodes. Due to the metallization of the CrI$_3$ layers that are adjacent to the Ag electrodes, B_i, C_i, and D_i are actually close to zero at the boundary. We will talk about this next.

c. Metallization effect.—First, we want to clarify that the metallized CrI$_3$ layer has stronger coupling with other neighboring CrI$_3$ layers due to enhanced interlayer exchange interactions from more itinerant electrons. Therefore, the metallization effect from the Ag electrodes not only affects the outermost layer, but can also be transmitted to the inner layers through enhanced interlayer coupling. However, this metallization effect from the electrodes diminishes rapidly, as it is transmitted to the inner layers due to the relatively large interlayer distance (3.59 Å) and the enhanced but still weak interlayer interaction. Thus, we can assume that the degree of metallization (defined as τ) of the CrI$_3$ layers, which reflects the effect of the Ag electrodes, is largest in the outermost layer, and

τ decreases rapidly as it gets closer to the innermost layer. So, when n is small, most of the CrI$_3$ layers are affected by the Ag electrodes. When n is large enough, the inner CrI$_3$ layers that are now in the majority are hardly affected by the Ag electrodes, and thus, behave the same, regardless of electrode type. The spin-filtering effect of the metallized CrI$_3$ layers that are in the minority is greatly diluted by that of the unaffected CrI$_3$ layers that are in the majority. Therefore, the effect of the electrodes becomes insignificant for large n.

We plot the spin-resolved PLDOS of the Ag-electrode MTJs with 2-layer, 5-layer, and 8-layer CrI$_3$ spacer layers in Figs. 9–11 to further explain the metallization effect. The Ag/2-layer CrI$_3$/Ag MTJ corresponds to the small-n case. As shown in Fig. 9, both CrI$_3$ layers are metallized and behave like magnetic metals, which filter the electrons with different spins according to the spin-resolved DOS at the Fermi level. The Ag/8-layer CrI$_3$/Ag MTJ corresponds to the large-n case. As shown in Fig. 11, the outermost two CrI$_3$ layers are greatly metallized (corresponding to maximal τ) and their adjacent 1–2 layers are also metallized, to a certain extent (white stripes near the Fermi level in Figs. 11(c) and 11(d), corresponding to limited τ). Whereas the innermost two CrI$_3$ layers are hardly affected by the Ag electrodes (corresponding to nearly zero τ) and behave the same, regardless of the electrode type.
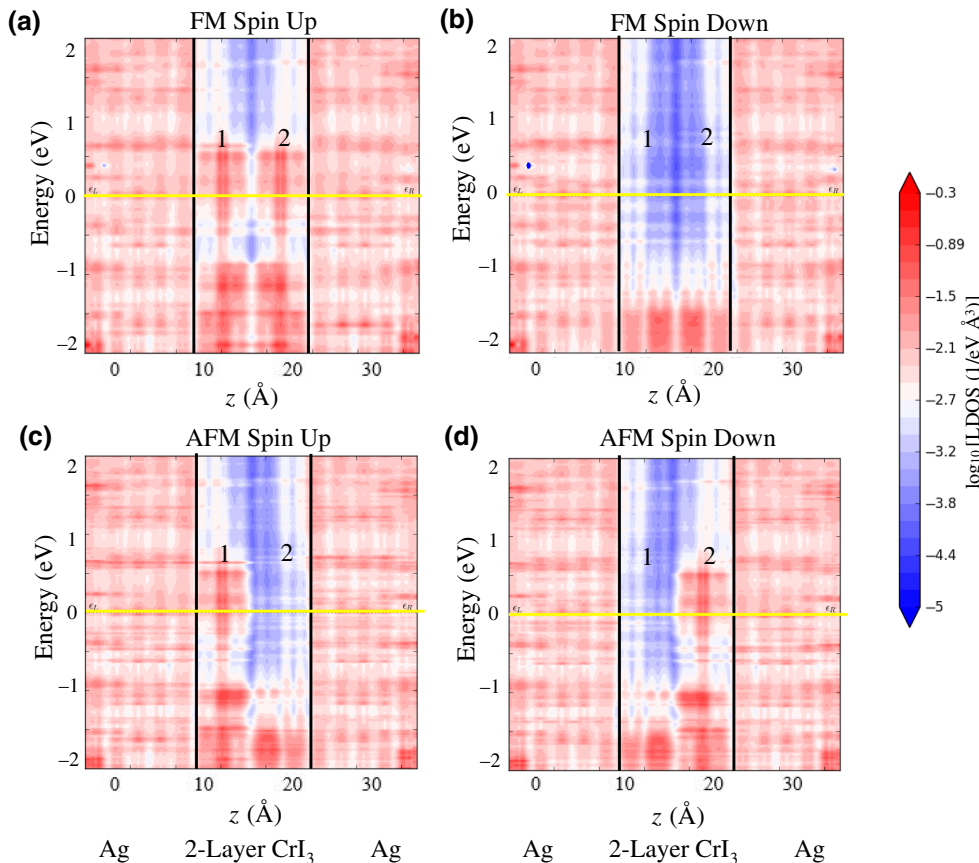

FIG. 9. Spin-resolved PLDOS of the Ag/2-layer CrI$_3$/Ag MTJ for the AFM and FM states. Fermi level is set to zero energy. Black lines indicate the boundary lines of the electrode and tunnel region, and yellow lines are the spin-dependent potential-barrier profiles. Numbers indicate the corresponding CrI$_3$ layers.
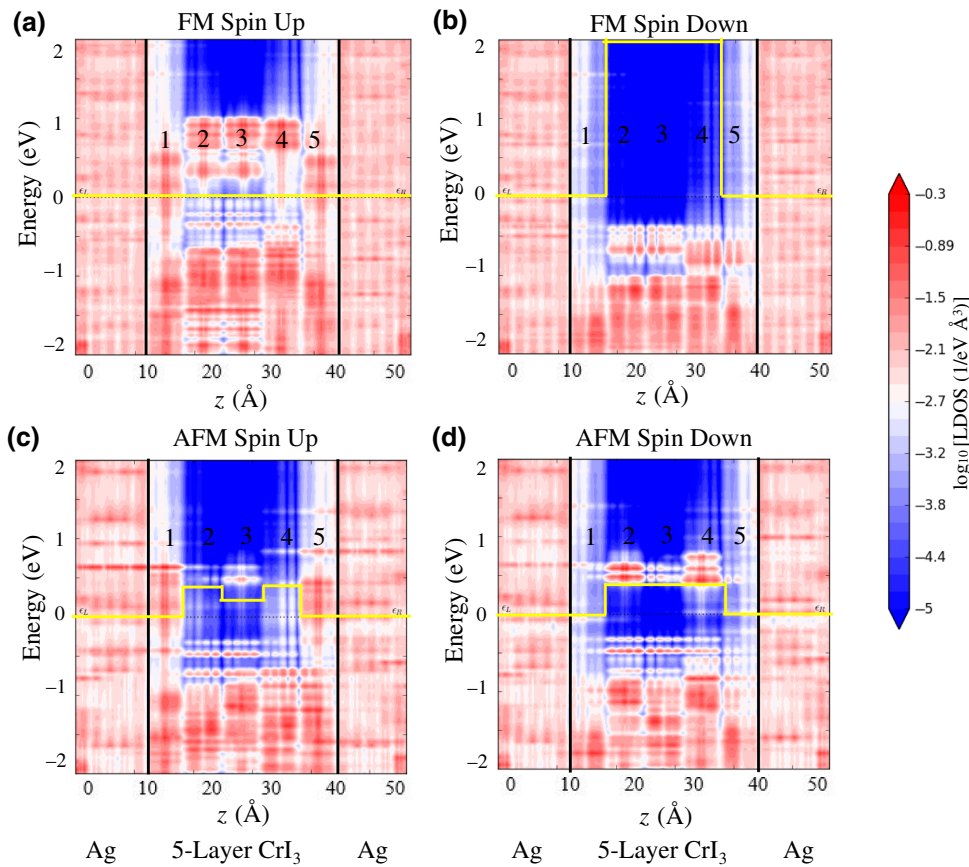
FIG. 10. Spin-resolved PLDOS of the Ag/5-layer CrI$_3$/Ag MTJ for the AFM and FM states. Fermi level is set to zero energy. Black lines indicate the boundary lines of the electrode and tunnel region, and yellow lines are the spin-dependent potential-barrier profiles. Numbers indicate the corresponding CrI$_3$ layers.

As n continues to increase, and when the contribution of the metallized part to overall transport is relatively small, the effect of the electrodes becomes insignificant.

d. Modification of the spin-filtering model.—First, we would like to emphasize that the previously used spin-filtering model is an approximation that treats each CrI$_3$ layer as an independent and identical tunnel barrier [29]. This model can help understand some basic phenomena, but it ignores the interlayer coupling and the effect of the electrodes. In our Ag/n-layer CrI$_3$/Ag MTJs, the interaction between the Ag electrodes and the adjacent CrI$_3$ layers is very strong, and the interlayer coupling of the CrI$_3$ layers is also enhanced due to the metallization effect, as we state above. So, we have to include these two factors to fully understand the complex phenomena. In fact, the conductance G and the SFE of the CrI$_3$ layers are both influenced by the degree of metallization, τ, and the interlayer coupling, which prevents the CrI$_3$ layers from being treated as equivalent tunnel barriers.

The effect of τ on G is easily comprehensible. A higher τ means more itinerant electrons near the Fermi level, and thus, larger G. The effect of τ on SFE can be comprehended in two extreme cases. When $\tau = 0$, which means the CrI$_3$ layer is not affected by the Ag electrodes,

we assume this CrI$_3$ layer has the highest SFE because of the spin-dependent tunneling process. As τ increases, which corresponds to the increasing DOS of the itinerant electrons near the Fermi level, the conductance of the spin-up ($G_\uparrow$) and spin-down electrons ($G_\downarrow$) both increase greatly. Because the original $G_\downarrow$ is several orders of magnitude smaller than the original $G_\uparrow$, the relative increase ratio of $G_\downarrow$ should be larger than that of $G_\uparrow$. Then, according to the definition of P, which can be written as $P = (G_\uparrow - G_\downarrow)/(G_\uparrow + G_\downarrow)$, if we multiply $G_\downarrow$ by a larger factor than the factor that we use to multiply $G_\uparrow$, at the same time, P decreases, which corresponds to the decrease of the SFE. When $\tau = 1$, which means the CrI$_3$ layer is completely transformed into a magnetic metal, we have to make it clear that, although the CrI$_3$ layer no longer works as a tunnel barrier, it still has the ability for spin filtering, just as 2D FM metals do. This feature is also verified by the different PLDOS of the spin-up and spin-down electrons in the highly metallized outermost CrI$_3$ layers shown in Figs. 9(c) and 9(d). The spin filtering of the 2D FM metals originates from the different DOS of the spin-up and spin-down electrons near the Fermi level, and the SFE of the 2D FM metals should be lower than that of the 2D FM semiconductors, according to our reasoning above. Previous experiments have also shown that P of the MTJ with 2D FM metal Fe$_3$GeTe$_2$ electrodes (7 layer and 21 layer) is
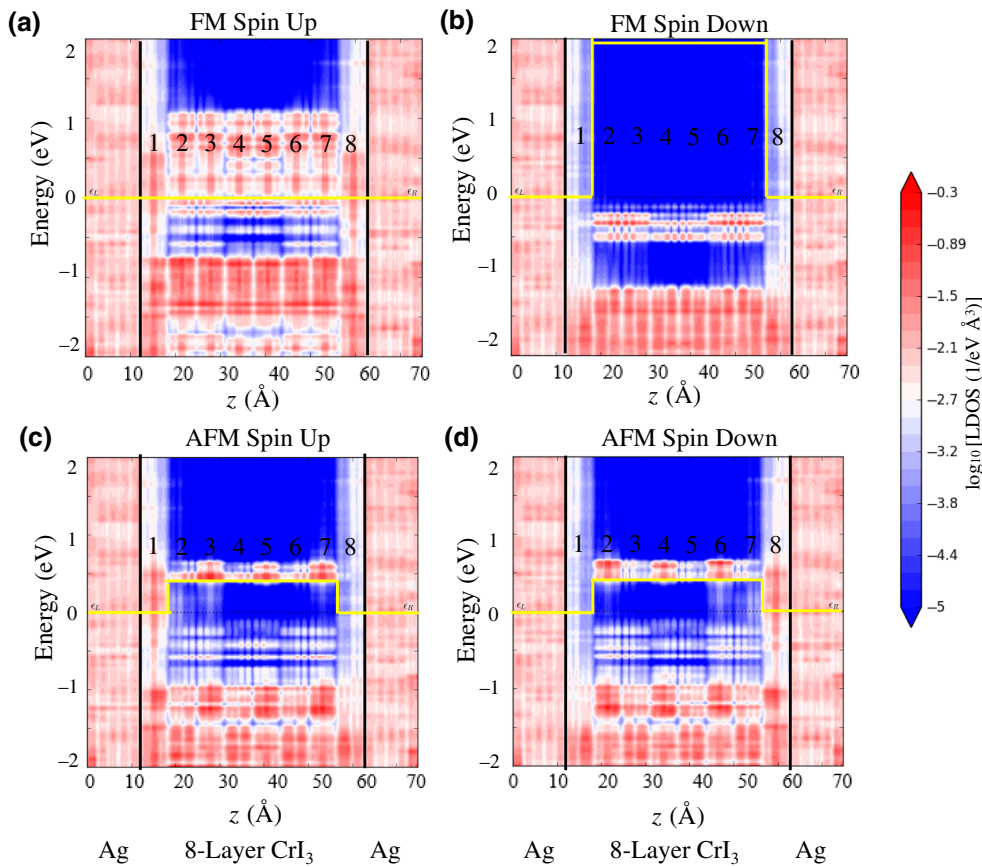
FIG. 11. Spin-resolved PLDOS of the Ag/8-layer CrI_3/Ag MTJ for the AFM and FM states. Fermi level is set to zero energy. Black lines indicate the boundary lines of the electrode and tunnel region, and yellow lines are the spin-dependent potential-barrier profiles. Numbers indicate the corresponding CrI_3 layers.

66% [25], which is lower than the experimental P value (99%) of the FM-ordered graphene/4-layer CrI_3/graphene MTJ [29]. This agrees with our conclusion. In summary, for the CrI_3 layers in the Ag-electrode MTJs, the larger the degree of metallization, τ, the larger the conductance, G, and lower the SFE. Notably, G changes greatly with τ, whereas SFE changes slightly.

Next, we consider the effect of interlayer coupling. Previous calculations have shown that, in the graphite/3-layer CrI_3/graphite MTJ, the $\uparrow\uparrow\downarrow$ (the arrows represent the relative out-of-plane magnetization directions of the corresponding CrI_3 layers) configuration exhibits larger conductance, G, than the $\uparrow\downarrow\uparrow$ configuration [57]. The reason for this difference is ascribed to the stronger magnetic coupling between the first two layers in the $\uparrow\uparrow\downarrow$ configuration, which leads to a conduction-band edge closer to the Fermi level for the spin-up electrons. In our Ag-electrode MTJs, the interlayer coupling is enhanced due to the metallization effect, as we state above. Therefore, the phenomenon that the coupling between CrI_3 layers with the same spin leads to larger conductance should also be more obvious. Actually, the behavior of G_{FM} in our out-of-plane-magnetized Ag/n-layer CrI_3/Ag MTJ at zero bias can be comprehended using this mechanism. G_{FM} remains relatively large ($\sim 10^{-2}$ e^2/h), even when the layer number is up to 12 and exhibits odd-even oscillation

with layer number n. By contrast, previous calculations have shown that G_{FM} of the Au/n-layer $CrPS_4$/Au MTJ decreases linearly and monotonically with n and reaches about 10^{-10} e^2/h when $n = 10$ [49]. The metallization effect of the Ag electrodes and enhanced coupling between the FM CrI_3 layers account for the relatively large G_{FM}. The odd-even oscillation of G_{FM} indicates that the coupling between CrI_3 layers with the same spin prefers pairwise pairing (possibly related to the A-B stacking mode), and the conductance of the two coupled CrI_3 layers is larger than that of an uncoupled single CrI_3 layer. Whereas, for G_{AFM}, the AFM-ordered configuration lacks the pairwise coupling of the adjacent same-spin CrI_3 layers (but there is probably secondary coupling between nonadjacent same-spin CrI_3 layers, which we will mention later). Therefore, G_{AFM} generally decreases with increasing n when $n < 8$. When $n \geq 8$, G_{AFM} exhibits odd-even oscillation, which means $G_{AFM,2l} > G_{AFM,2l-1}$ where l is a positive integer and $2l \geq 8$. We assume the reason might be that, when n is a large even number, the two adjacent CrI_3 layers with opposite spins can be combined to be treated as a fundamental unit and then couple with each other. This coupling resembles the coupling between adjacent same-spin CrI_3 layers (as the $\uparrow\downarrow$ units are nearly the same, if we ignore the metallization effect when n is large), and thus, can also improve the conductance.

Then, according to the definition of TMR, which can be written as TMR $= \frac{G_{FM} - G_{AFM}}{G_{AFM}} = \frac{G_{FM}}{G_{AFM}} - 1$, we can comprehend the behavior of TMR from the relative change between G_{FM} and G_{AFM}. When $n < 8$, the odd-even oscillation of the TMR is the result of combining the odd-even oscillation of G_{FM} and the monotonic decreasing of G_{AFM}. Meanwhile, the combination of the reduced decreasing rate of G_{AFM} and the relatively larger decreasing rate of G_{FM} when $n = 3$, 5, and 7 leads to the relatively low TMR. When $n \geq 8$, G_{FM} and G_{AFM} exhibit odd-even oscillation at the same time. Notably, the relative change rate of G_{FM} [i.e., $(G_{FM, n} - G_{FM, n-1})/(G_{FM, n-1})$] is larger than that of G_{AFM} [i.e., $(G_{AFM, n} - G_{AFM, n-1})/(G_{AFM, n-1})$] when n is even, and the situation is opposite when n is odd ($n \geq 8$). In other words, when the conductance increases due to coupling (either between adjacent CrI_3 layers or between $\uparrow\downarrow$ units), G_{FM} increases faster than G_{AFM}. When the conductance decreases due to one extra layer, G_{AFM} decreases faster than G_{FM}. This is actually a sign that the coupling between adjacent same-spin CrI_3 layers is stronger than the coupling between adjacent $\uparrow\downarrow$ units. This difference leads to the monotonic increasing of the TMR when $n \geq 8$.

Here, we explain why we do not pursue TMR beyond 12 CrI_3 layers. Our calculation results show that the conductance, G, generally decreases with increasing n in the CrI_3-based MTJs. Notably, our Ag-electrode MTJ is a special case, as G_{FM} remains relatively large ($\sim 10^{-4}$ e^2/h), even when the layer number is up to 11 due to the metallization effect of the Ag electrodes and enhanced coupling between the CrI_3 spacer layers. By contrast, G_{AFM} is already reduced to about 10^{-11} e^2/h when n reaches 11. We have also mentioned that G_{FM} of the Au/10-layer $CrPS_4$/Au MTJ is about 10^{-10} e^2/h [49]. We assume that the general decreasing tendency of G with increasing n will not change. Then too small a conductance will result in many problems. First, when G is too small, the calculation will be beyond our precision. For example, our calculated G of the graphite/4-layer CrI_3/graphite MTJ reaches about 10^{-24} e^2/h, and, when we increase n to 5, we find that the calculation is already beyond our precision. At the same time, too large an n also means more atoms and will exceed our computational ability. Second, in practical experiments, if G is too small, the measuring current will also be too small to distinguish. Previous experiments show that the minimum current in the graphite/10-layer CrI_3/graphite MTJ already reaches 1 pA [25]. Therefore, when n is very large, the theoretically predicted large TMR cannot be measured by experimental means, which means this prediction loses its practical value. Third, a low resistance-area product (RA), which is related to impedance matching, and power-consumption reduction are required for MTJs [58]. Too small a G means a very large RA, which also prevents the practical application of MTJs. Finally, if we want to downscale the device size, we also have to control the

thickness of the spacer layer, which means that n cannot be too high. For the above reasons, we choose a suitable range of n to conduct our calculations and do not pursue TMR beyond 12 CrI_3 spacer layers. In addition to having a large TMR, the most suitable n for practical applications should also consider other factors, including appropriate G and RA.

To finish clarifying the effect of interlayer coupling on G and TMR, we now explain the effect of interlayer coupling on the SFE. Previous calculations have shown that, in the graphite/n-layer CrI_3/graphite MTJ, they have $P_\uparrow \approx 0.79$, $P_{\uparrow\uparrow} \approx 0.92$, $P_{\uparrow\uparrow\uparrow} \approx 0.94$, $P_{\uparrow\uparrow\downarrow} \approx 0.73$, and $P_{\uparrow\downarrow\uparrow} \approx 0.35$ (the arrows represent the relative out-of-plane magnetization directions of the corresponding CrI_3 layers) [57]. The difference between $P_\uparrow$ and $P_{\uparrow\downarrow\uparrow}$ indicates that the spin filtering of two adjacent CrI_3 layers with opposite spins cannot simply cancel each other out. The difference between $P_{\uparrow\uparrow\downarrow}$ and $P_{\uparrow\downarrow\uparrow}$ indicates that the coupling between two adjacent CrI_3 layers with the same spin can greatly improve the SFE, which resembles the phenomenon that this coupling leads to an improvement of G.

After modifying the simplest spin-filtering model with the metallization effects of the Ag electrodes and enhanced interlayer coupling, we now get back to the variation tendency of P_{AFM} in our out-of-plane-magnetized Ag/n-layer CrI_3/Ag MTJ at zero bias. For the even-layer configurations like $\uparrow\downarrow\uparrow\downarrow \ldots \uparrow\downarrow\uparrow\downarrow$, even if we consider the metallization effect and the interlayer coupling, the overall device is still symmetric for both spins. Therefore, the sum of the spin filtering of all the CrI_3 layers for the spin-up and spin-down electrons is still the same, which leads to the near-zero $P_{AFM,even}$. For the odd-layer configurations like $\uparrow\downarrow\uparrow \ldots \uparrow\downarrow\uparrow$, when n is small (typically less than seven), all the CrI_3 layers are metallized, to a certain extent, and the interlayer coupling is greatly enhanced. Although the two CrI_3 layers with the same spin are not adjacent, there is probably still a certain degree of coupling between them that helps improve P_{AFM} when $n = 3$ and 5. To be specific, when $n = 3$, this coupling refers to the coupling between the first layer and the third layer, which are also the two outermost layers with the highest τ, and thus, the strongest coupling. When $n = 5$, the situation is similar and the coupling between the first layer and the fifth layer is probably not very weak because all the CrI_3 layers are metallized, to a certain extent. The significantly reduced decreasing rate of G_{AFM} when $n = 3$ and 5 also suggests the probable existence of coupling between nonadjacent same-spin layers because this coupling can also lead to an improvement in G. When n is large, more unmetallized layers appear in the middle and coupling between nonadjacent same-spin CrI_3 layers (especially the coupling between the two outermost same-spin layers that contributes most to the improved $P_{AFM,odd}$ when $n = 3$ and 5) is blocked. At the same time, spin filtering of one specific CrI_3 layer is diluted by the spin filtering of all the other CrI_3 layers. Therefore, $P_{AFM,odd}$

gradually decreases with increasing *n* and approaches zero when *n* is large enough.

3. $k_\parallel$-resolved transmission of the out-of-plane-magnetized Ag/*n*-layer CrI₃/Ag MTJ at zero bias

For a more comprehensive understanding of the spin-dependent tunneling process, we also plot $k_\parallel$-resolved transmission of the Ag/*n*-layer CrI₃/Ag MTJs with out-of-plane magnetization at zero bias for the FM and AFM states in the 2D Brillouin zone (BZ) from $n = 3$ to $n = 10$, as shown in Fig. 12. An intuitive first impression is that the transmission coefficients of the FM state are generally more significant than those of the AFM state, and the difference in the order of magnitude generally increases

with the layer number, judging from the scale bar, which also leads to the general increasing of TMR. The distribution of the red area in the 2D BZ for the FM state is generally different from that for the AFM state, except for $n = 3$ and $n = 5$. The different distributions in 2D BZ represent different tunnel channels and partly account for the huge TMR. When $n = 3$ and $n = 5$, the distributions for both states are very similar, despite the numerical difference. This corresponds to the approximate 100% P_{AFM} when $n = 3$ and $n = 5$, as we explain above.

4. Bias effects

The calculated TMR values of the graphite/n-layer CrI₃/graphite MTJs at zero bias are much larger than Klein's experimental values [29] at zero bias and Song's
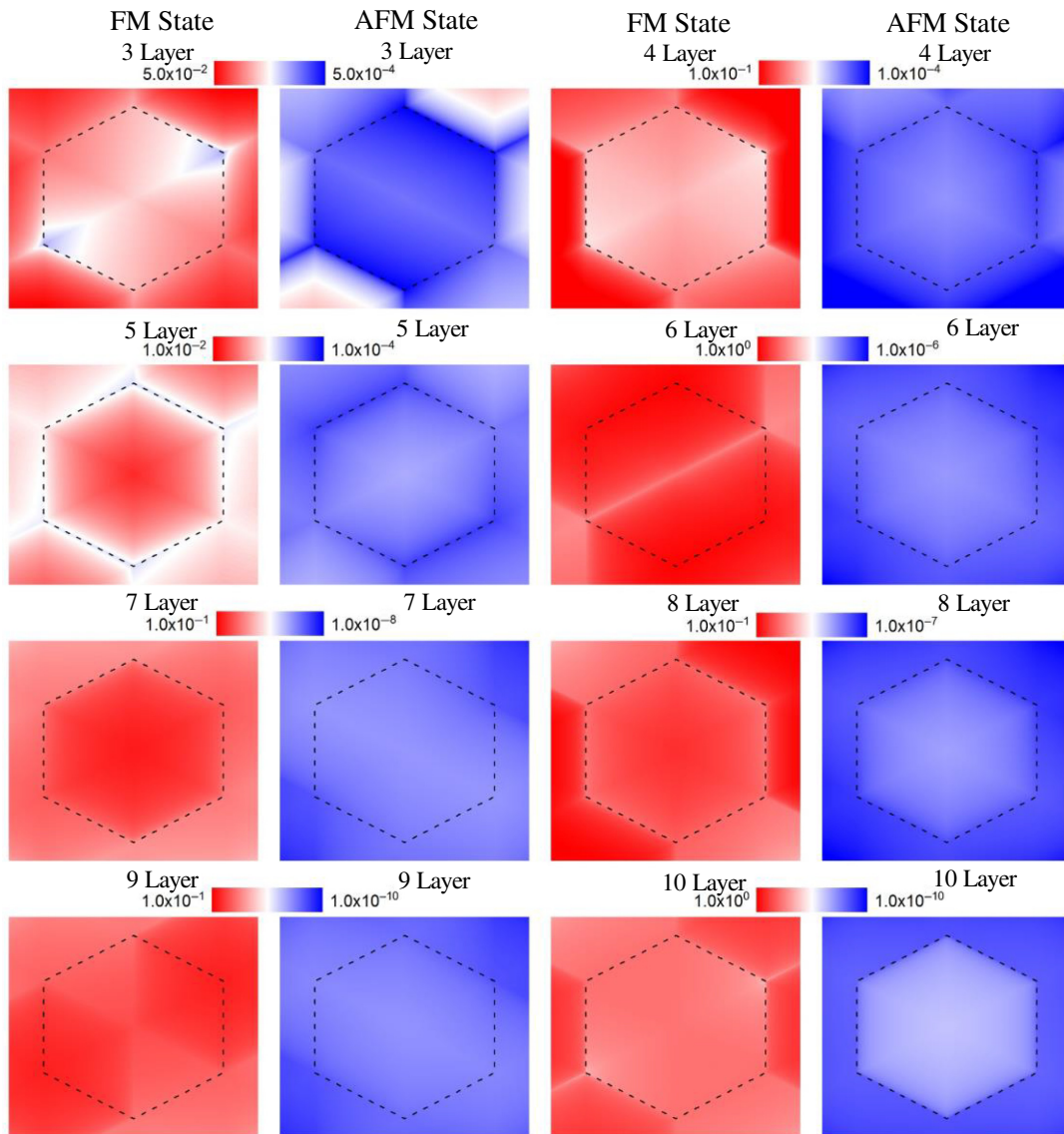

FIG. 12. $k_\parallel$-resolved transmission coefficients across the Ag/*n*-layer CrI₃/Ag (*n* is from 3 to 10) magnetic tunnel junction in the Brillouin zone (dashed line) for the FM and AFM states calculated at the Fermi level.
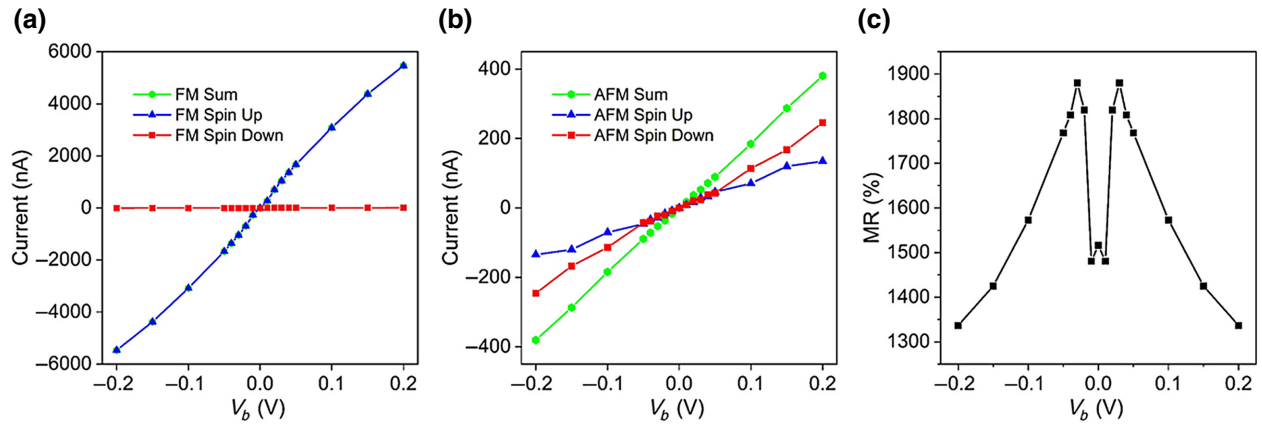
FIG. 13. Bias voltage dependence of the spin-resolved current for the FM state (a), the AFM state (b), and the TMR (c) in the Ag/2-layer CrI_3/Ag MTJ.

experimental values at zero bias [30], but close to Song's largest TMR values at $V_b \approx 0.3$ V. The difference between the two experimental results is probably due to the effect of such detailed conditions as the detailed interfacial quality, measuring temperature, and applied bias [8]. The calculated values at zero bias are much larger than the experimental values at zero bias because the calculations are carried out under ideal conditions, including absolutely flat surfaces and zero temperature.

In terms of the applied bias voltage, the calculation results and Klein's experimental results [23] are both obtained under zero bias voltage, while Song's largest TMR is obtained under $V_b \approx 0.3$ V [24]. To determine the effect of the bias voltage on the TMR, we calculate the spin-resolved current and the TMR of the Ag/2-layer CrI_3/Ag MTJ with out-of-plane magnetization under different bias voltages, as shown in Fig. 13. As the bias voltage, V_b, increases from zero, the spin-resolved current generally keeps increasing. In the FM-ordered

configuration, the spin-up current is much larger than the spin-down current, while, in the AFM-ordered configuration, the spin-up and spin-down currents are very similar. With increasing V_b, the TMR first slightly decreases from 1510% to 1480% and then increases until $V_b = 0.03$ V, where the TMR reaches the maximum value of 1880%. After that, the TMR monotonically decreases with increasing V_b, and the whole tendency is similar to that in Song's experiment using graphite electrodes [30].

5. Magnetization-direction effects

In Song's experiment, we notice that the TMR of the in-plane-magnetized configuration is generally larger than that of the out-of-plane magnetized configuration. So, we perform noncollinear spin-polarized transport calculations in the in-plane magnetized graphite/n-layer CrI_3/graphite MTJs to determine the noncollinear spin-orientation effect. As shown in Fig. 14(a), the transmission coefficients
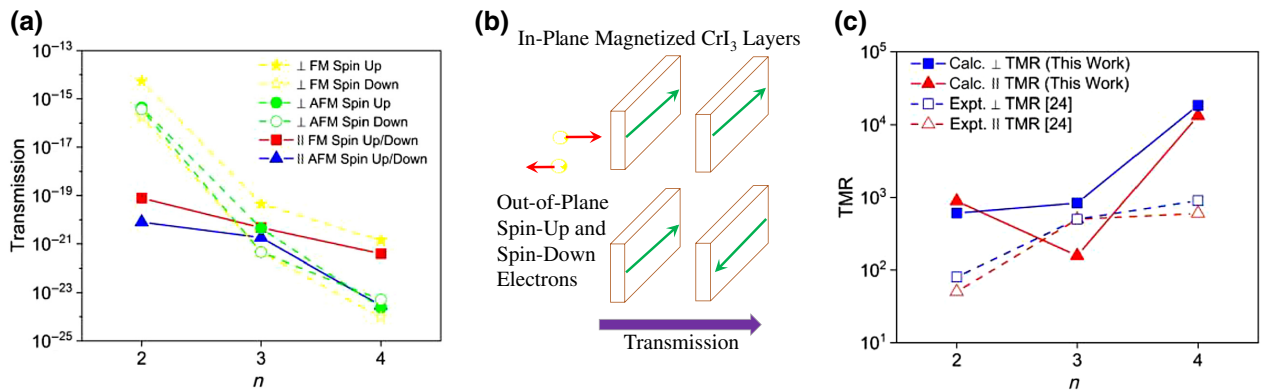

FIG. 14. (a) Comparison of the transmission function at $E_f = 0$ eV between the in-plane and out-of-plane-magnetized graphite/n-layer CrI_3/graphite MTJs at zero bias. (b) Schematic model of the noncollinear transport process. Red arrows represent the spin orientation of the electrons, and green arrows represent the magnetization direction of the CrI_3 layers. (c) Same as (a) but for TMR at zero bias.

of spin-up and spin-down electrons are exactly degenerate in the in-plane-magnetized CrI_3 layer because the incoming out-of-plane-magnetized spin-up and spin-down electrons are symmetric for the in-plane-magnetized CrI_3 layers, as shown in Fig. 14(b). Furthermore, the transmission coefficients monotonically decrease with increasing n, and those of the FM-ordered configurations are larger than those of the AFM-ordered configurations. In addition, compared with the transmission coefficients in the out-of-plane-magnetized configurations, the transmission coefficients in the in-plane-magnetized configurations are several orders of magnitude smaller when $n = 2$, and the difference becomes smaller as n increases. When $n = 4$, the transmission coefficients in the in-plane- and out-of-plane-magnetized configurations are very similar.

Now we turn to the TMR results. As shown in Fig. 14(c), compared with the collinear (out-of-plane) situation, the calculated TMR in the in-plane-magnetized configuration is slightly larger when $n = 2$ ($880\% > 600\%$) but slightly smaller when $n = 3$ ($160\% < 830\%$) and $n = 4$ ($13\,000\% < 18\,000\%$). In Song's experiment, the TMR at zero bias in the in-plane-magnetized configuration is close to that in the out-of-plane-magnetized configuration when $n = 3$ [30]. When $n = 2$ and 4, the TMR values at zero bias in the in-plane-magnetized configuration are smaller than those in the out-of-plane-magnetized configuration [30]. The reduction tendency of the TMR in the in-plane-magnetized configuration coincides with our calculation results.

IV. CONCLUSION

We first summarize the scaling behavior of spin-resolved band gaps of n-layer CrI_3 and find that the variation range of all the spin-resolved band gaps is relatively small (less than 0.2 eV). Then we investigate the scaling behavior of TMR of the Ag/n-layer CrI_3/Ag MTJ with layer numbers over a large range (from 2 to 12 layer) at zero bias with out-of-plane magnetization, and a generally increasing trend of TMR with the tunnel-barrier layer number, n, is revealed, that is, from 200% (2 layer) to an incredible $10^9\%$ value (12 layer). Specifically, when $n < 7$, the variation trend of TMR exhibits odd-even oscillation, and the TMR monotonously increases from $n = 7$ to $n = 12$. We also calculate the TMR of the graphite/n-layer CrI_3/graphite MTJ from 2 to 4 layers at zero bias with out-of-plane magnetization, and a monotonously increasing trend of the TMR is obtained, which corresponds with the experimental results. Furthermore, the TMR of the Ag/2-layer CrI_3/Ag MTJ under increasing bias voltage is found to slightly decrease from 1510% to 1480%, when $V_b = 0.01$ V, and then increases until $V_b = 0.03$ V, where TMR reaches a maximum value of 1880%. Additionally, compared with the collinear (out-of-plane) situation, the calculated

TMR of the in-plane-magnetized MTJs with graphite electrodes is slightly larger when $n = 2$ ($880\% > 600\%$) but slightly smaller when $n = 3$ ($160\% < 830\%$) and $n = 4$ ($13\,000\% < 18\,000\%$). The reduction tendency of the TMR in the in-plane-magnetized configuration coincides with the experimental results. Our results will motivate further explorations of 2D-magnet-based MTJs.

[1] S. Ikeda, J. Hayakawa, Y. Ashizawa, Y. M. Lee, K. Miura, H. Hasegawa, M. Tsunoda, F. Matsukura, and H. Ohno, Tunnel magnetoresistance of 604% at 300 K by suppression of Ta diffusion in CoFeB/MgO/CoFeB pseudo-spin-valves annealed at high temperature, Appl. Phys. Lett. **93**, 082508 (2008).

[2] M. F. Khan, H. Kim, G. Nazir, S. Jung, and J. Eom, Layer dependent magnetoresistance of vertical MoS_2 magnetic tunnel junctions, Nanoscale **10**, 16703 (2018).

[3] H. Dery, P. Dalal, L. Cywinski, and L. J. Sham, Spin-based logic in semiconductors for reconfigurable large-scale circuits, Nature **447**, 573 (2007).

[4] L. Pan, L. Huang, M. Zhong, X. W. Jiang, H. X. Deng, J. Li, J. B. Xia, and Z. Wei, Large tunneling magnetoresistance in magnetic tunneling junctions based on two-dimensional CrX3 (X = Br, I) monolayers, Nanoscale **10**, 22196 (2018).

[5] B. Behin-Aein, D. Datta, S. Salahuddin, and S. Datta, Proposal for an all-spin logic device with built-in memory, Nat. Nanotechnol. **5**, 266 (2010).

[6] A. A. Tulapurkar, Y. Suzuki, A. Fukushima, H. Kubota, H. Maehara, K. Tsunekawa, D. D. Djayaprawira, N. Watanabe, and S. Yuasa, Spin-torque diode effect in magnetic tunnel junctions, Nature **438**, 339 (2005).

[7] J. C. S. S. I. Kiselev, I. N. Krivorotov, N. C. Emley, R. J. Schoelkopf, R. A. Buhrman, and D. C. Ralph, Microwave oscillations of a nanomagnet driven by a spin-polarized current, Nature **425**, 380 (2003).

[8] C. Gong and X. Zhang, Two-dimensional magnetic crystals and emergent heterostructure devices, Science **363**, 706 (2019).

[9] M. Gibertini, M. Koperski, A. F. Morpurgo, and K. S. Novoselov, Magnetic 2D materials and heterostructures, Nat. Nanotechnol. **14**, 408 (2019).

[10] M. Long, P. Wang, H. Fang, and W. Hu, Progress, challenges, and opportunities for 2D material based photodetectors, Adv. Funct. Mater. **29**, 1803807 (2019).

[11] T. McGuire and R. Potter, Anisotropic magnetoresistance in ferromagnetic 3d alloys, IEEE Trans. Magn. **11,** 1018 (1975).

[12] M. N. Baibich, J. M. Broto, A. Fert, F. N. Van Dau, F. Petroff, P. Etienne, G. Creuzet, A. Friederich, and J. Chazelas, Giant Magnetoresistance of (001)Fe(001)Cr Magnetic Superlattices, Phys. Rev. Lett. **61,** 2472 (1988).

[13] S. Yuasa and D. D. Djayaprawira, Giant tunnel magnetoresistance in magnetic tunnel junctions with a crystalline MgO(0 0 1) barrier, J. Phys. D: Appl. Phys. **40,** R337 (2007).

[14] J. S. M. a and G. Mathon, Spin polarized tunneling in ferromagnetic junctions, J. Magn. Magn. Mater. **200,** 248 (1999).

[15] S. Schmaus, A. Bagrets, Y. Nahas, T. K. Yamada, A. Bork, M. Bowen, E. Beaurepaire, F. Evers, and W. Wulfhekel, Giant magnetoresistance through a single molecule, Nat. Nanotechnol. **6,** 185 (2011).

[16] H. Fukuzawa, H. Yuasa, S. Hashimoto, H. Iwasaki, and Y. Tanaka, Large magnetoresistance ratio of 10% by $Fe_{50}Co_{50}$ layers for current-confined-path current-perpendicular-to-plane giant magnetoresistance spin-valve films, Appl. Phys. Lett. **87,** 082507 (2005).

[17] A. Voskoboynikov, S. S. Liu, and C. P. Lee, Spin-dependent electronic tunneling at zero magnetic field, Phys. Rev. B **58,** 15397 (1998).

[18] V. I. Perel', S. A. Tarasenko, I. N. Yassievich, S. D. Ganichev, V. V. Bel'kov, and W. Prettl, Spin-dependent tunneling through a symmetric semiconductor barrier, Phys. Rev. B **67,** 201304 (2003).

[19] S. A. Tarasenko, V. I. Perel, and I. N. Yassievich, In-Plane Electric Current is Induced by Tunneling of Spin-Polarized Carriers, Phys. Rev. Lett. **93,** 056601 (2004).

[20] P. S. Alekseev, M. M. Glazov, and S. A. Tarasenko, Spin injection via (110)-grown semiconductor barriers, Phys. Rev. B **89,** 155306 (2014).

[21] P. S. Alekseev, V. M. Chistyakov, and I. N. Yassievich, Electric-field effect on the spin-dependent resonance tunneling, Semiconductors **40,** 1402 (2006).

[22] J. Moser, A. Matos-Abiague, D. Schuh, W. Wegscheider, J. Fabian, and D. Weiss, Tunneling Anisotropic Magnetoresistance and Spin-Orbit Coupling in Fe/GaAs/Au Tunnel Junctions, Phys. Rev. Lett. **99,** 056601 (2007).

[23] K. S. Burch, D. Mandrus, and J. G. Park, Magnetism in two-dimensional van der waals materials, Nature **563,** 47 (2018).

[24] M. Bonilla, S. Kolekar, Y. Ma, H. C. Diaz, V. Kalappattil, R. Das, T. Eggers, H. R. Gutierrez, M. H. Phan, and M. Batzill, Strong room-temperature ferromagnetism in VSe_2 monolayers on van der waals substrates, Nat. Nanotechnol. **13,** 289 (2018).

[25] Z. Wang, D. Sapkota, T. Taniguchi, K. Watanabe, D. Mandrus, and A. F. Morpurgo, Tunneling spin valves based on Fe_3GeTe_2/hBN/Fe_3GeTe_2 van der waals heterostructures, Nano Lett. **18,** 4303 (2018).

[26] B. Huang, G. Clark, E. Navarro-Moratalla, D. R. Klein, R. Cheng, K. L. Seyler, D. Zhong, E. Schmidgall, M. A. McGuire, D. H. Cobden, W. Yao, D. Xiao, P. Jarillo-Herrero, and X. Xu, Layer-dependent ferromagnetism in a van der waals crystal down to the monolayer limit, Nature **546,** 270 (2017).

[27] C. Gong, L. Li, Z. Li, H. Ji, A. Stern, Y. Xia, T. Cao, W. Bao, C. Wang, Y. Wang, Z. Q. Qiu, R. J. Cava, S. G. Louie, J. Xia, and X. Zhang, Discovery of intrinsic ferromagnetism in two-dimensional van der waals crystals, Nature **546,** 265 (2017).

[28] D. J. O'Hara, T. Zhu, A. H. Trout, A. S. Ahmed, Y. K. Luo, C. H. Lee, M. R. Brenner, S. Rajan, J. A. Gupta, D. W. McComb, and R. K. Kawakami, Room temperature intrinsic ferromagnetism in epitaxial manganese selenide films in the monolayer limit, Nano Lett. **18,** 3125 (2018).

[29] D. R. Klein, D. MacNeill, J. L. Lado, D. Soriano, E. Navarro-Moratalla, K. Watanabe, T. Taniguchi, S. Manni, P. Canfield, J. Fernández-Rossier, and P. Jarillo-Herrero, Probing magnetism in 2D van der waals crystalline insulators via electron tunneling, Science **360,** 1218 (2018).

[30] T. C. Song, X. H. Cai, M. W. Y. Tu, X. O. Zhang, B. V. Huang, N. P. Wilson, K. L. Seyler, L. Zhu, T. Taniguchi, K. Watanabe, M. A. McGuire, D. H. Cobden, D. Xiao, W. Yao, and X. D. Xu, Giant tunneling magnetoresistance in spin-filter van der waals heterostructures, Science **360,** 1214 (2018).

[31] H. H. Kim, B. Yang, T. Patel, F. Sfigakis, C. Li, S. Tian, H. Lei, and A. W. Tsen, One million percent tunnel magnetoresistance in a magnetic van der waals heterostructure, Nano Lett. **18,** 4885 (2018).

[32] B. Huang, G. Clark, D. R. Klein, D. MacNeill, E. Navarro-Moratalla, K. L. Seyler, N. Wilson, M. A. McGuire, D. H. Cobden, D. Xiao, W. Yao, P. Jarillo-Herrero, and X. Xu, Electrical control of 2D magnetism in bilayer CrI_3, Nat. Nanotechnol. **13,** 544 (2018).

[33] S. Jiang, J. Shan, and K. F. Mak, Electric-field switching of two-dimensional van der waals magnets, Nat. Mater. **17,** 406 (2018).

[34] L. Pan, H. Wen, L. Huang, L. Chen, H.-X. Deng, J.-B. Xia, and Z. Wei, Two-dimensional XSe2 (X = Mn, V) based magnetic tunneling junctions with high curie temperature, Chin. Phys. B **28,** 107504 (2019).

[35] Y. Wang, S. Liu, Q. Li, R. Quhe, C. Yang, Y. Guo, X. Zhang, Y. Pan, J. Li, H. Zhang, L. Xu, B. Shi, H. Tang, Y. Li, J. Yang, Z. Zhang, L. Xiao, F. Pan, and J. Lu, Schottky barrier heights in two-dimensional field-effect transistors: From theory to experiment, Rep. Prog. Phys. **84,** 056501 (2021).

[36] T. R. Paudel and E. Y. Tsymbal, Spin filtering in CrI_3 tunnel junctions, ACS Appl. Mater. Interfaces **11,** 15781 (2019).

[37] Z. Yan, R. Zhang, X. Dong, S. Qi, and X. Xu, Significant tunneling magnetoresistance and excellent spin filtering effect in CrI_3-based van der waals magnetic tunnel junctions, Phys. Chem. Chem. Phys. **22,** 14773 (2020).

[38] H. Zhou, Y. Zhang, and W. Zhao, Tunable tunneling magnetoresistance in van der waals magnetic tunnel junctions with 1T-$CrTe_2$ electrodes, ACS Appl. Mater. Interfaces **13,** 1214 (2021).

[39] N. D. Mermin and H. Wagner, Absence of Ferromagnetism or Antiferromagnetism in one- or 2-Dimensional Isotropic Heisenberg Models, Phys. Rev. Lett. **17,** 1133 (1966).

[40] J. P. Perdew, K. Burke, and M. Ernzerhof, Generalized Gradient Approximation Made Simple, Phys. Rev. Lett. **77,** 3865 (1996).

[41] P. E. Blochl, Projector augmented-wave method, Phys. Rev. B **50,** 17953 (1994).

[42] G. Kresse and D. Joubert, From ultrasoft pseudopotentials to the projector augmented-wave method, Phys. Rev. B **59,** 1758 (1999).

[43] G. Kresse and J. Hafner, Ab-initio molecular-dynamics for open-shell transition-metals, Phys. Rev. B **48,** 13115 (1993).

[44] Y. Guo, B. Wang, X. Zhang, S. Yuan, L. Ma, and J. Wang, Magnetic two-dimensional layered crystals meet with ferromagnetic semiconductors, InfoMat **2,** 639 (2020).

[45] M. Brandbyge, J. L. Mozos, P. Ordejon, J. Taylor, and K. Stokbro, Density-functional method for nonequilibrium electron transport, Phys. Rev. B **65,** 165401 (2002).

[46] J. M. Soler, E. Artacho, J. D. Gale, A. Garcia, J. Junquera, P. Ordejon, and D. Sanchez-Portal, The SIESTA method for ab initio order-N materials simulation, J. Phys. Condens. Matter **14,** 2745 (2002).

[47] Y. Wang, J. Zheng, Z. Ni, R. Fei, Q. Liu, R. Quhe, C. Xu, J. Zhou, Z. Gao, and J. Lu, Half-metallic silicene and germanene nanoribbons: Towards high-performance spintronics device, NANO **07,** 1250037 (2012).

[48] B. Wu, R. Quhe, J. Yang, S. Liu, J. Shi, J. Lu, and H. Du, High-performance spin filters and spin field effect transistors based on bilayer VSe_2, Adv. Theory Simul. **4,** 2000238 (2020).

[49] J. Yang, S. Fang, Y. Peng, S. Liu, B. Wu, R. Quhe, S. Ding, C. Yang, J. Ma, B. Shi, L. Xu, X. Sun, G. Tian, C. Wang, J. Shi, J. Lu, and J. Yang, Layer-Dependent Giant Magnetoresistance in Two-Dimensional $CrPS_4$ Magnetic Tunnel Junctions, Phys. Rev. Appl. **16,** 024011 (2021).

[50] C. Yang, Z. Song, X. Sun, and J. Lu, Valley pseudospin in monolayer $MoSi_2N_4$ and $MoSi_2As_4$, Phys. Rev. B **103,** 035308 (2021).

[51] D. Supriyo, *Quantum Transport: Atom to Transistor* (Cambridge University Press, New York, the United states of America, 2005).

[52] N. Liu, S. Zhou, and J. Zhao, High-Curie-temperature ferromagnetism in bilayer CrI_3 on bulk semiconducting substrates, Phys. Rev. Mater. **4,** 094003 (2020).

[53] A. K. Kundu, Y. Liu, C. Petrovic, and T. Valla, Valence band electronic structure of the van der waals ferromagnetic insulators: VI_3 and CrI_3, Sci. Rep. **10,** 15602 (2020).

[54] V. Tran, R. Soklaski, Y. Liang, and L. Yang, Layer-controlled band gap and anisotropic excitons in few-layer black phosphorus, Phys. Rev. B **89,** 235319 (2014).

[55] C.-W. Hu, Y. Yang, C. Hou, and T.-X. Liang, Thickness- and strain-tunable electronic structures of two-dimensional Bi_2O_2Se, Comput. Mater. Sci. **194,** 110424 (2021).

[56] W. B. Zhang, Q. Qu, P. Zhu, and C. H. Lam, Robust intrinsic ferromagnetism and half semiconductivity in stable two-dimensional single-layer chromium trihalides, J. Mater. Chem. C **3,** 12457 (2015).

[57] J. J. Heath, M. Costa, M. Buongiorno-Nardelli, and M. A. Kuroda, Role of quantum confinement and interlayer coupling in CrI_3-graphene magnetic tunnel junctions, Phys. Rev. B **101,** 195439 (2020).

[58] X. Li, Y. Su, M. Zhu, F. Zheng, P. Zhang, J. Zhang, and J.-T. Lü, Current-Perpendicular-to-Plane Giant Magnetoresistance Effect in van der Waals Heterostructures, Phys. Rev. Appl. **16,** 034052 (2021).